



Influence of Friction Stir Spot Processing on Grain Structure Evolution and Nanomechanical Behavior of Cold-Sprayed Al Coating on Ti Substrate

Gang Ji^{1,2} · Xin-Yuan Dong³ · Long-Shi Qiu¹ · Xiao-Gang Hu¹ · Hong Liu² · Xiao-Tao Luo² · Cheng-Xin Li²

Submitted: 28 May 2024 / in revised form: 20 July 2024 / Accepted: 29 July 2024
© ASM International 2024

Abstract The grain structure evolution and nanomechanical behavior of cold-sprayed Al coating on Ti substrate with friction stir spot processing (FSSP) were studied by the electron backscatter diffraction and nanoindentation methods. The low-angle boundaries (LAGBs) fraction and the density of the geometrically necessary dislocations (GNDs) decreased from the base zone (BZ) to the stir zone (SZ). The average grain size, the LAGBs fraction and the density of the GNDs were various in different locations of the SZ, which can be attributed to the variety of local shear strain and temperature gradient during FSSP. The B/\bar{B} component, the C component, and the A_1^*/A_2^* component were mainly developed in the SZ. The highest intensity of the B/\bar{B} component appeared in the 3/8D of the SZ, indicating that the plasticized materials flowed downward experienced the highest shear strain. The materials in the heat affected zone (HAZ) underwent static recrystallization, while the continuous dynamic recrystallization (CDRX) and the geometric dynamic recrystallization (GDRX) occurred in the thermo-mechanically affected zone (TMAZ) and SZ. The nano-hardness and elastic modulus of the cold-sprayed Al coating after FSSP were comparable to those of pure Al bulk. The grain size and

dislocation density were the main factors affecting the nano-hardness in the SZ.

Keywords cold spray · friction stir spot processing · grain structure · nanomechanical behavior · texture

Introduction

Cold spray is a solid-state coating technology applied to produce coatings with low-oxide content (Ref 1, 2). Meanwhile, because of the residual compressive stress produced by the impact of high-velocity particles (Ref 3), a thick cold-sprayed coating can be readily developed under optimal spraying conditions. For the past few years, cold spraying technology has been widely applied to the preparation of Al and its alloy coatings (Ref 4-9). Since the gas can be readily trapped between the particles during the spraying and the depositions are achieved with solid particles, it is difficult to obtain completely dense Al and its alloy coatings that have good inter-particle bonding, which decreases its mechanical, electrical and corrosion performance (Ref 5, 6).

Many methods have been utilized to densify the pure Al and its alloy coatings and increase the inter-particle bonding (Ref 6-10). Generally, higher particle velocity and temperature are beneficial to obtain denser layer (Ref 11). Balani et al. (Ref 6) employed helium as the accelerating gas to prepare the pure Al coatings, where dense coatings were developed, and the corrosion resistance of the coatings was enhanced. However, helium is too expensive to employ as the accelerating gas. Adding a certain mass of hard second-phase particles into Al feedstock powder is a common way to densify the cold-sprayed coatings. The damping effect of the hard second-phase particles to the

✉ Long-Shi Qiu
qiuls88@126.com

¹ Xi'an Rare Metal Materials Institute Co., Ltd.,
Xi'an 710016, Shaanxi, China

² State Key Laboratory for Mechanical Behavior of Materials,
School of Materials Science and Engineering, Xi'an Jiaotong
University, Xi'an 710049, Shaanxi, China

³ AECC Commercial Aircraft Engine Co., Ltd,
Shanghai 200241, China

deposited Al particles facilitates the densification of the coatings (Ref 7). Nevertheless, it should be noted that the bonding mechanism of the particles is still the mechanical interlocking, which reduces the mechanical properties of the coating. Heat treatment is another widely applied method to eliminate the pores in the coating and improve the interface bonding through solid-state diffusion. Bu et al. (Ref 8) investigated the interface structure of cold-sprayed Al coatings on Mg alloy after heat treatment, demonstrating that thick intermetallic compounds appeared between the cold-sprayed Al coating and Mg alloy substrate. Huang et al. (Ref 9) studied the mechanical properties of cold-sprayed coatings after heat treatment. The defects in the cold-sprayed Al coatings were gradually fixed at higher temperature, which modified the tensile strength and the ductility of the coatings. However, it could not be ignored that the growth of grains would lower the properties of the annealed coatings (Ref 12).

Nowadays, a solid-state technique, friction stir processing (FSP) was used to modify the cold-sprayed Al coatings (Ref 10). During the process, a rotating tool is plunged into the Al coatings and then moves along the surface of the coatings. The voids and the inter-particle interfaces are absent while the coatings and the substrates are mixed well after FSP, suggesting that the FSP is a potential technology to improve the cold-sprayed Al coatings (Ref 13-15). Wang et al. (Ref 16) used FSP to modified the cold-sprayed oxide dispersion strengthened (ODS) steel plate, pointing out that the strength-ductility tradeoff of the cold-sprayed ODS steel plate became excellent after FSP due to the fully dense microstructure and the refinement and redistribution of nano-sized oxide particles. Han et al. (Ref 17) modified the cold-sprayed CoCrFeNi HEA coating by FSP, suggesting that the mechanical properties of the coating were improved attributed to low porosity combined with high interface bonding. Khodabakhshi et al. (Ref 18) applied FSP to process the cold-sprayed Ti coating on Al substrate, where the absence of pores and inter-particle interfaces enhanced the hardness of the coating. Moreover, it is well known that FSP leads to the formation of particular textures and fine recrystallized grains in the stir zone (SZ), which will strongly influence the material properties after FSP. Khodabakhshi et al. (Ref 19) reported that the deformed crystallographic textural component was dominated in the SZ of the cold-sprayed Ti coating after FSP. However, the relationship between the texture and properties of the coating was not been elucidated. Meanwhile, to the best of the author's knowledge, few studies have reported the texture evolution and dynamic recrystallization behavior of the cold-sprayed Al coatings during FSP.

It should be noted that the research on FSW of Al and Al alloys can enlighten the study of the texture and grain structure evolution of cold-sprayed Al coatings modified by

FSP. In the research of R.W. Fonda et al. (Ref 20), the appearance of refined grain in the SZ was thought to be induced by the deformation and the dynamic recovery processes. Suhuddin et al. (Ref 21) discussed the grain structure and texture development during FSW of 6016 aluminum, finding that the mechanism of microstructure evolution varied at different positions from the tool. Meanwhile, as S. Chen et al. (Ref 22) described, grain refinement development was dominated by strain induced boundary migration mechanism and GDRX during FSW of 2219 aluminum. And Cube {001} <100>, Goss {011} <100>, Brass {011} <211> and Cube ND {001} <110> developed in the thermo-mechanically affected zone (TMAZ), the heat affected zone (HAZ) and the SZ, which did not follow the simple shear texture. Shen et al. (Ref 23) investigated the microstructural development during refill friction stir spot welding of the AlMgSc alloy. The textural pattern was determined as the A_1^*/A_2^* component in the weld center and the B/\bar{B} component in the other regions. The evolution of the refined grains was supposed to be driven by GDRX and continuous dynamic recrystallization (CDRX). Therefore, it is necessary to accurately judge the texture and recrystallization form of cold-sprayed Al coatings after FSP, so as to obtain the relationship between microstructure and properties.

As a linear processing technique, FSP is not suitable for processing the coatings on curved surfaces and in small areas. Therefore, for more flexible modification of coatings on curved surfaces and in small areas, friction stir spot processing (FSSP), based on FSP, was applied to modify the cold-sprayed pure Al coating. The texture evolution and grain recrystallization of the cold-sprayed Al coating during FSSP was studied in detail. Moreover, the influence of texture and grain structure on the nanomechanical of the coating was illustrated.

Experimental Procedures

Cold-Sprayed Deposition

The feedstock powders utilized in this study were the pure spherical Al particles prepared by the gas atomization without heat treatment, and the size of the particles were around 35 μm . The pure titanium (TA2) sheets of 3 mm thickness were used as substrates. To enhance the adhesion between the substrate and coating, the substrate was grit-blasted using Al_2O_3 grits before spraying. A custom-developed cold-sprayed system (CS-2000, Xi'an Jiaotong University, China) was employed to perform deposition. Nitrogen was applied as the accelerating gas at a pressure of 3 MPa and a temperature of around 230 $^\circ\text{C}$. The nozzle

standoff distance was 20 mm and the gun traverse speed was set to 40 mm/s. The thickness of pure Al deposits was about 1.6 mm and ground to around 1.5 mm.

FSSP Treatment

The FSSP was carried out on a commercial friction stir welding machine (LQH-G15, Weihai lianqiao precision machinery Co., Ltd., PR China). The processing rotation speed of 2400 rpm was employed, a plunge rate of 1 mm/min, a plunge depth of 0.5 mm, and a dwell time of 20 s were performed to modify the cold-sprayed Al coating. The H13 steel tool with a diameter of 16 mm had six involute grooves machined on the tool surface, as given in Fig. 1.

Materials Characterization

The macrostructure was examined with an optical microscope (OM, Nikon MA200, Japan). The scanning electron microscope (SEM, MIRA 3 LMH, TESCAN, Czech) equipped with an EBSD system was used to examine the microstructural development. The samples for OM observation were sectioned through their centers, prepared by standard metallurgical procedures, and etched using a solution containing 1 mL of hydrofluoric acid, 1.5 mL of hydrochloric acid, 2.5 mL of nitric acid, and 95 mL of water. The samples for EBSD analysis were prepared by standard metallurgical procedures followed by ion polishing (Leica EM RES102, PR China). The EBSD data were acquired at an accelerating voltage of 15 kV under a step size of 0.6 μm . In the maps presented in this paper, the fine lines in silver denote the low-angle boundaries (LAGBs) with misorientation angles between 2 and 15 $^\circ$ and the thick lines in black represent the high-angle boundaries (HAGBs) with misorientation angles exceeding 15 $^\circ$. The

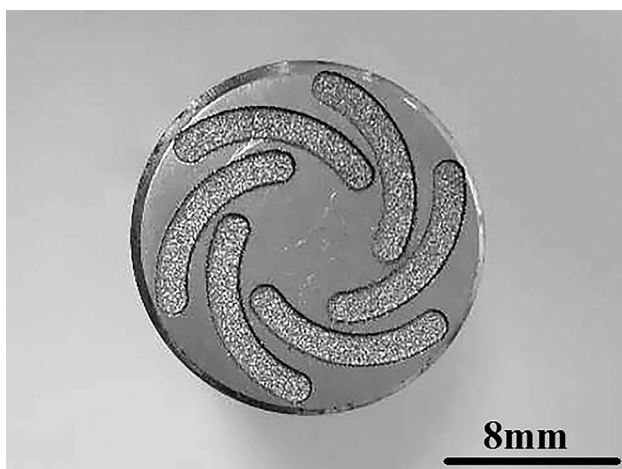


Fig. 1 Schematic of the FSSP tool geometry

sample coordinate system is defined by the transverse and normal directions (TD, ND) which can be seen in Fig. 2.

Nanoindentation Analysis

The nanoindentation test was performed at the top, middle, and bottom of the 1/2D of the SZ, and the 1/4D of the SZ using nanomechanical testing system (TI950 Triboindenter). The 'D' presented in Fig. 2b represents the diameter of the processing zone. The Berkovich indenter was chosen and the analysis surface was ND \times TD plane as given in Fig. 2. The test was carried out at peak load of 5000 μN with a holding time of 2 s, while the loading and unloading time was set at 15 s. At least three indents were averaged to calculate the mean nano-hardness and elastic modulus values and synthesize the load-displacement curve.

Result and Discussion

Microstructure Evolution at Different Locations After FSSP

Figure 2 gives the macrostructure of the cross section of the cold-sprayed Al coating before and after FSSP. As shown in Fig. 2a, the contrast of the as-deposited coating is resemblant in the whole area, implying the uniform distribution of the inter-particle boundaries and the pores in the coating. However, the contrast of the coating is diverse in different locations of the coating after FSSP as given in Fig. 2b, which may be the result of the varying degree of particle deformation in different locations of the coating after FSSP. In this research, the processing zone of the cold-sprayed Al coating is classified into four zones, namely base zone (BZ), HAZ, TMAZ, and SZ. The BZ is close to the HAZ and outside the range of the diameter of the tool. The HAZ is within the diameter of the tool, where the heat effect is much greater than the mechanical effect. EBSD dates were carried out in the BZ, the HAZ, the TMAZ, and the SZ from the selected locations, which are indicated in Fig. 2b. For comparison, a location in the as-deposited Al coating was also selected for EBSD analysis.

Figure 3 shows the inverse pole figure (IPF) and the kernel average misorientation (KAM) maps in the as-deposited Al coating and the BZ, the HAZ, and the TMAZ of the cold-sprayed Al coating after FSSP. In the IPF maps, the grains were colored according to their crystallographic orientation, as presented by the orientation code triangle at the left bottom corner. The KAM value reflects the density of geometrically necessary dislocations (GNDs) in a local area, and a high KAM value indicates that a large number of dislocations piled up there (Ref 24–26). The average grain sizes and LAGBs fractions for different locations of

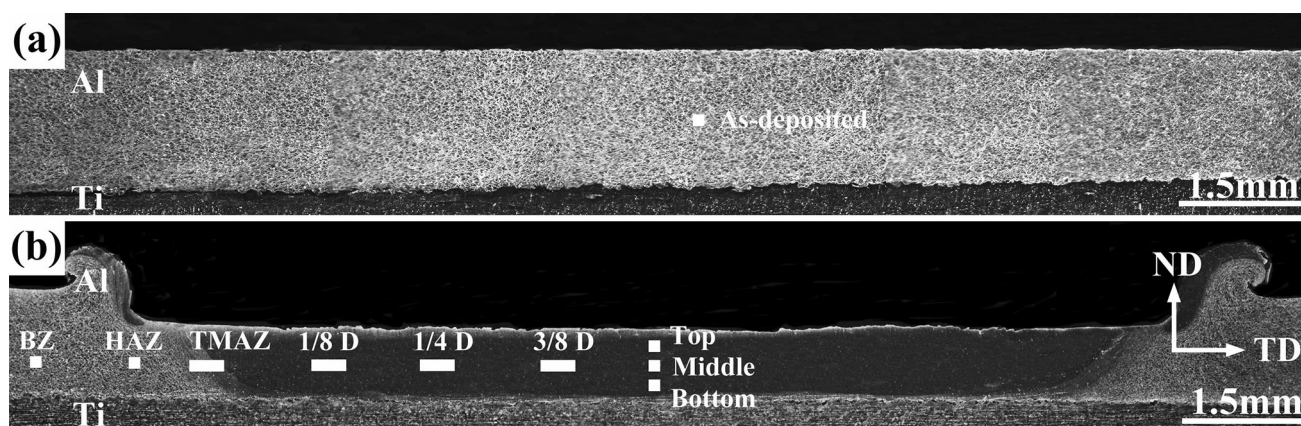


Fig. 2 Macrostructure of the cross section of the cold-sprayed Al coating (a) before and (b) after FSSP

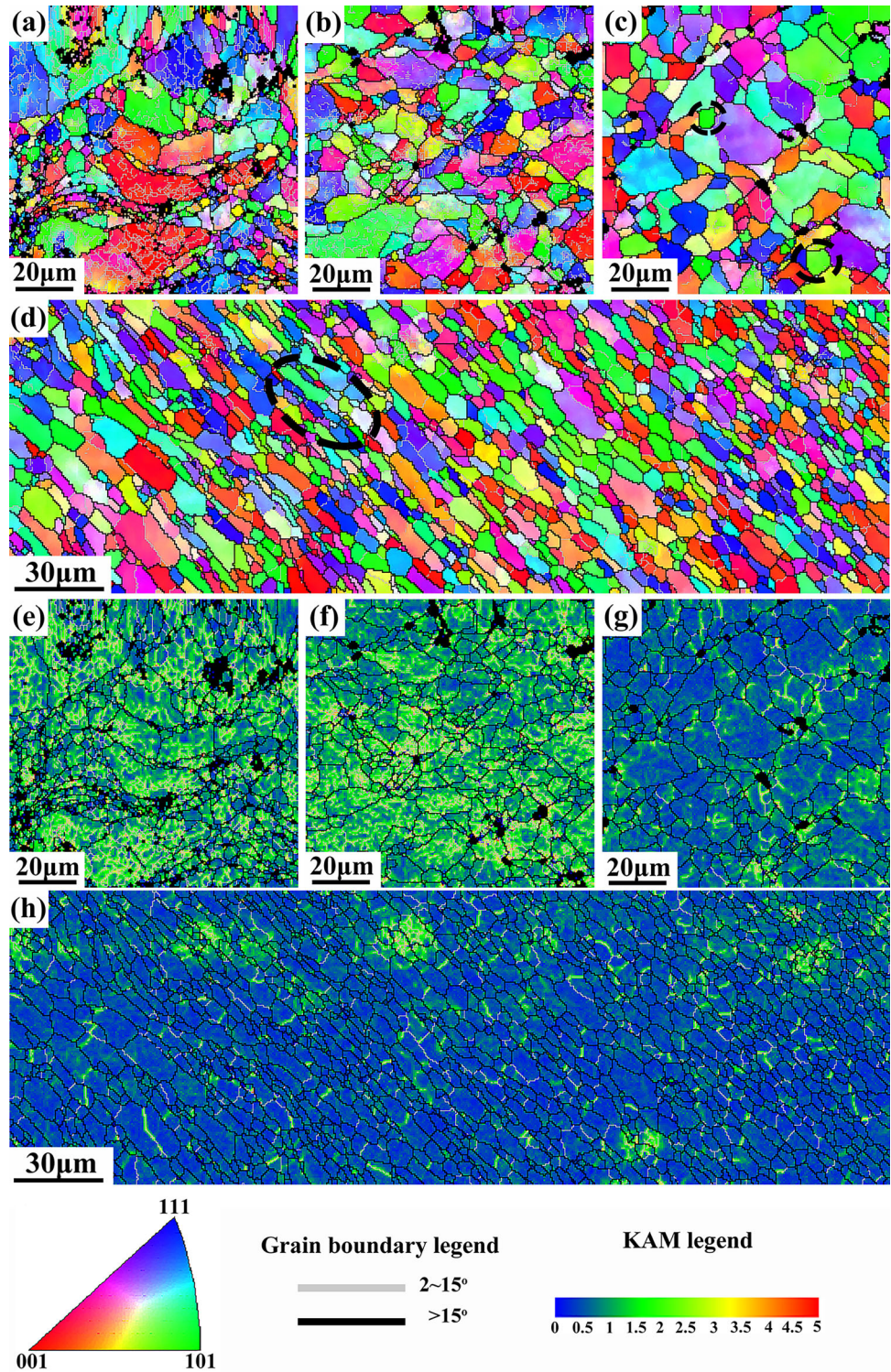
the cold-sprayed Al coatings before and after FSSP are given in Table 1. As can be seen in Fig. 3a, owing to the inhomogeneous deformation across the entire particle (Ref 27), the grains with various sizes are unevenly distributed in the as-deposited coating, and a large fraction of LAGBs within the sub-grains can be observed. Meanwhile, the KAM values are relatively high in the as-deposited Al coating as given in Fig. 3e, which suggests that a large number of GNDs store up in this location due to the intense plastic deformation of the particles. These massive GNDs could form dislocation cells that develop sub-grains (Ref 28). Figure 3b is the IPF of the BZ in the cold-sprayed Al coating after FSSP. The growth of ultrafine grains occurs due to the influence of thermal action. However, a large number of LAGBs remain in the grains. The KAM value is relatively high which means that the heat propagated into the BZ is not enough to reduce the GNDs as can be observed in Fig. 3f. Under the influence of the heat generated by the tool, the grains grow further in the HAZ, which is given in Fig. 3c. The KAM value drops dramatically, indicating that a large number of GNDs are eliminated in the HAZ (Fig. 3g). Figure 3d shows that the TMAZ has grains with mixed features, i.e., equiaxed and fibrous, which is usually considered as a feature of partial recrystallization. The equiaxed grains increase in the area near the stirring zone, and the KAM value maintains at a very low level shown in Fig. 3h.

Figure 4 presents the IPF and the KAM maps in the 1/8D, 1/4D, and 3/8D of the SZ. Fig. 4a-c show that the equiaxed grains containing a small amount of LAGBs can be observed in these three locations. It can be noticed that the sheared directions of the equiaxed grains are different in these three locations, which may be the result of the material flow mode of the FSSP. The grain sizes of these three locations are almost the same, as given in Table 1. The KAM values are very low in these three locations, indicating that the dislocation annihilation occurs and the

dislocation density decreases as given in Fig. 4d-f. However, some grains with high KAM value are present in some areas of the 1/4D of the SZ marked by white ellipses in Fig. 4e, meaning the aggregation of high-density GNDs. The material flow can influence the recrystallization process (Ref 23). When the areas were subjected to minimal shear strain, the driving force for recrystallization was relatively small, and the recrystallization kinetics were stagnated, resulting in high KAM values in these areas.

Figure 5 shows the IPF and the KAM maps in the top, middle, and bottom of the 1/2D of the SZ. The grains are remarkably recrystallized in the 1/2D of the SZ as presented in Fig. 5a-c. However, the grain size distribution is not homogeneous throughout the thickness of the SZ. The average grain sizes in the top, middle, and bottom locations of the SZ are about 2.5 μm , 3.8 μm and 4.1 μm , respectively. The variation of grain size in the SZ is probably due to the different extents of deformation in the specific location during FSSP and the temperature gradient through the thickness of the SZ after FSSP. The material in the top of the SZ undergoes severe plastic deformation during FSSP, which makes the grains have the strongest tendency to recrystallize. Therefore, the average grain sizes are finer in the top of the SZ. The grains in the bottom were subjected to minimal plastic deformation during FSSP. However, due to the poor thermal conductivity of the Ti substrate, the bottom location keeps high temperature for a longer time compared with other locations after FSSP, leading to the growth of the grains. The KAM values are relatively low in the top and bottom of the 1/2D of the SZ, indicating the presence of low density of the GNDs, which are visible in Fig. 5d-f. Nevertheless, the higher GNDs density (higher KAM value) occurs in the middle of the 1/2D of the SZ as given in Fig. 5e. It can be noticed that the trend of the LAGBs fraction is the same as that of the KAM values from the top to the bottom of the 1/2D of the SZ. During FSSP, the local shear strain is sufficient in the top

Fig. 3 IPF and KAM maps in (a, e) the as-deposited Al coating and (b, f) the BZ, (c, g) the HAZ, (d, h) the TMAZ of the cold-sprayed Al coating after FSSP



of the coating, and the recrystallization kinetics are fast, resulting in low density of the GNDs. However, due to the inability of insufficient local shear strain to sufficiently reduce the GNDs, the temperature gradient would play an important role in decreasing the density of the GNDs in the bottom of the SZ after FSSP (Ref 29). Owing to the low

thermal conductivity of the Ti substrate, a high-temperature gradient would appear in the coating after FSSP. The bottom of the SZ would stay at high temperature for a longer time, leading to the dislocation annihilation.

Table 1 Average grain sizes and LAGBs fractions for different locations of the cold-sprayed Al coatings before and after FSSP

Locations	Average grain size, μm	LAGBs fraction, percent
As-deposited coating	1.92	30.5
BZ	2.47	25.8
HAZ	3.7	11.1
TAMZ	3.3	10.5
1/8D of the SZ	3.7	9.8
1/4D of the SZ	3.8	9.6
3/8D of the SZ	3.5	9.7
Top of the 1/2D of the SZ	2.5	9.6
Middle of the 1/2D of the SZ	3.8	10.1
Bottom of the 1/2D of the SZ	4.1	9.5

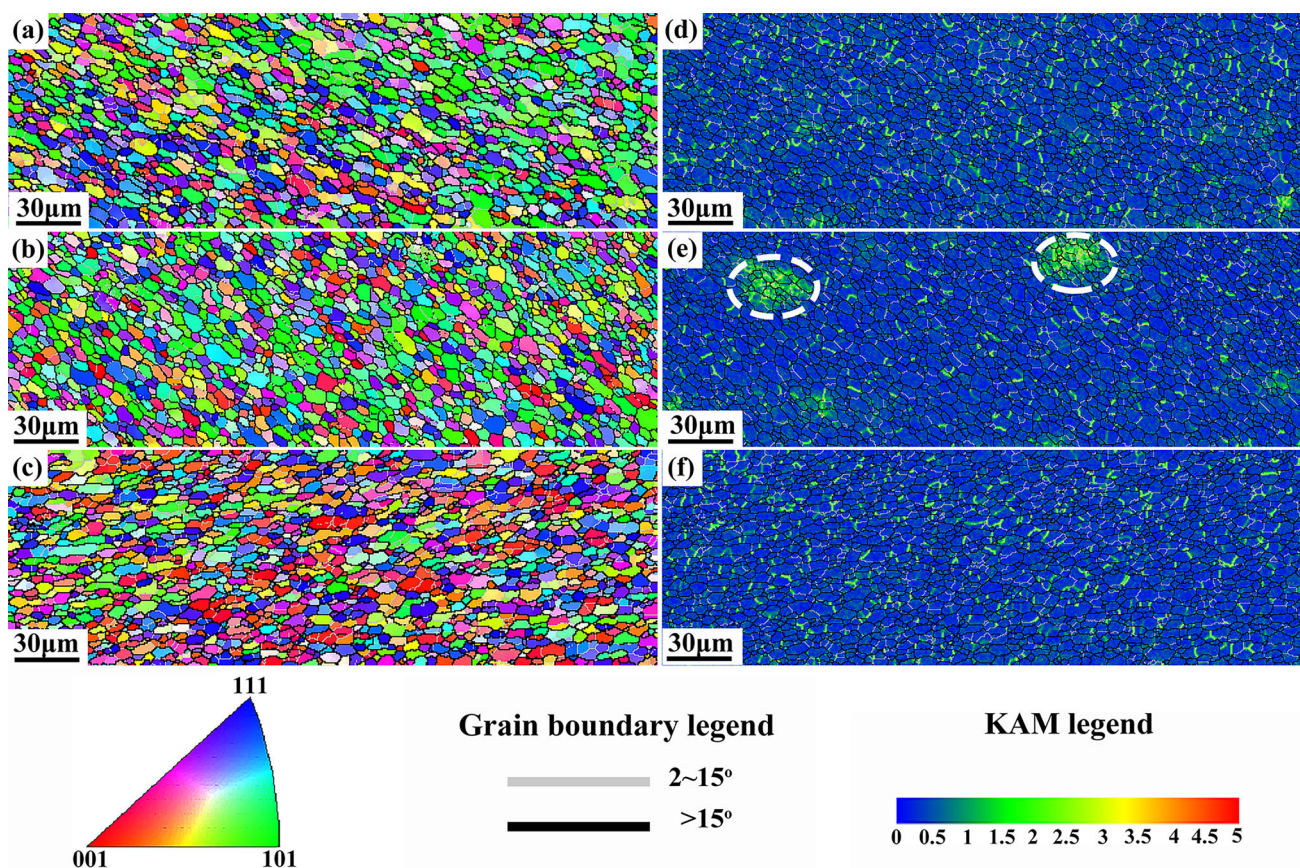


Fig. 4 IPF and the KAM maps in the (a, d) 1/8D, (b, e) 1/4D, and (c, f) 3/8D of the SZ

Texture Evolution at Different Locations in the SZ After FSSP

During FSSW, the physical process is consistent with the simple shear, which applies the simple shear frame. Thus, the rotation route is employed to rearrange the pole figures (PFs) to align with the SPN vertically and the SD horizontally. Then, to separate the components that partially overlapped in the PFs, the $\varphi_2 = 0^\circ$ and $\varphi_2 = 45^\circ$ sections from the orientation distribution function (ODF)

with triclinic symmetry using Bunge notations are presented as well. The unit of multiples of uniform density (MUD) is shown at the bottom of the ODFs, indicating the strength of the clustering of a specific orientation. The locations of the ideal components of a simple shear texture for FCC metals are indicated in Fig. 6 (Ref 30).

Figure 7 shows the PFs and ODFs in the 1/8D, 1/4D, and 3/8D of the SZ. It can be seen that the B/\bar{B} component is developed in these three locations, while minor C component and the A^*_1/A^*_2 component appear in the 1/4D of

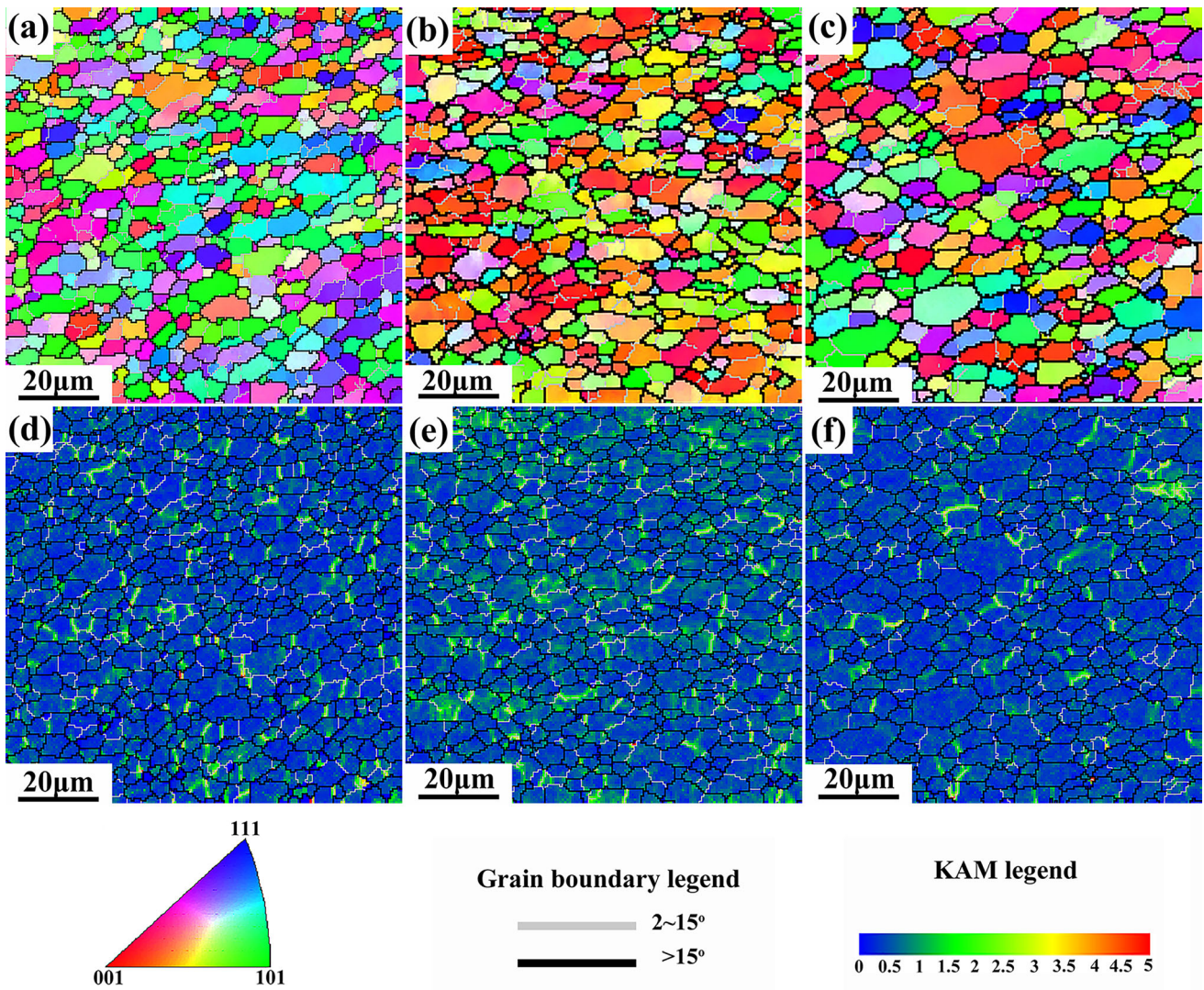


Fig. 5 IPF and the KAM maps in the (a, d) top, (b, e) middle, and (c, f) bottom of the 1/2D of the SZ

the SZ. The intensity of the B/\bar{B} component is the lowest in the 1/4D of the SZ, and is the highest in the 3/8D of the SZ. The texture components developing in these three locations are shown in Fig. 8, which applies highlight data that contain a particular texture. A user-defined color scheme shown as color key reflects how close the data is to this texture. Specific grain boundary maps of these three locations were also superimposed in the texture component maps. The max deviation is set as 20° . As seen from Fig. 8, most B/\bar{B} grains contain in the 3/8D of the SZ. Even though only the B/\bar{B} component develops in the 1/8D and 3/8D of the SZ in the PFs, extremely few A^*_1/A^*_2 grains, A/\bar{A} grains and C grains can be observed in these three locations as presented in Fig. 8a and c.

Figure 9 shows the PFs and ODFs in the top, middle and bottom of the 1/2D of the SZ. It can be observed that the B/\bar{B} component is mainly developed in the top and middle.

The C component is mainly developed in the bottom, where minor A^*_1/A^*_2 component appears. The strength of the B/\bar{B} component is the highest in top of the SZ. Figure 10 demonstrates the texture components developed in these three locations. As can be seen in Fig. 10a-b, a large number of B/\bar{B} grains appear in the top and middle of the SZ, where few A^*_1/A^*_2 grains, A/\bar{A} grains and C grains are also observed. Figure 10c presents that C grains are more certain to appear in the bottom of the SZ.

The difference of the texture developments in the different locations of the SZ are most likely related to the local shear strain, which means that the magnitude of the simple shear strain directly correlated with the texture components (Ref 31, 32). In summary, the A^*_1/A^*_2 component dominates at lower strain. The A/\bar{A} component predominates at low strains but will be replaced by the C component as the strain increase. When the strains reach to

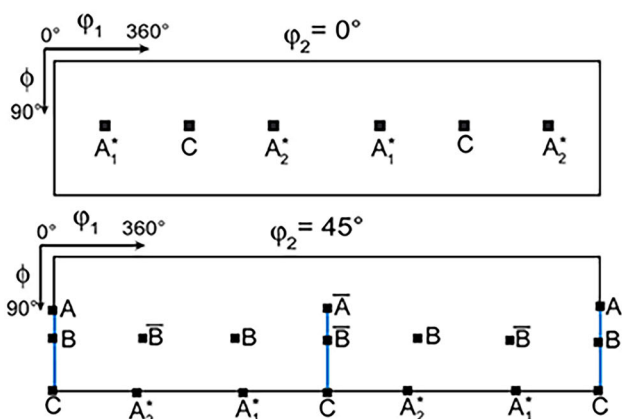
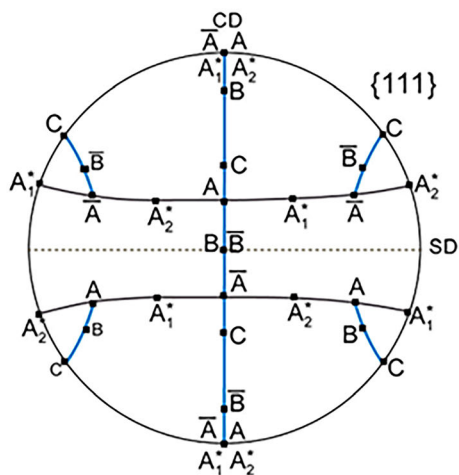


Fig. 6 Locations of the ideal components of a simple shear texture for FCC metals

3-5, the B/\bar{B} component appear. As the strains increase to 10-20, nearly entire of the B/\bar{B} component will emerge. Therefore, for the materials in the 1/8D, 1/4D and 3/8D of the SZ, they are subject to different shear strains which are related to the material flow mode at different locations. The plasticized material that flows downward in the 3/8D of the SZ (Fig. 4c) undergoes the highest strain, and that flows outward in the 1/8D of the SZ (Fig. 4a) experiences the lowest strain. Comparing the texture component in the top, middle and bottom of the 1/2D of the SZ, the plasticized material in the top undergoes the highest strain due to its proximity to the tool, while the material in the bottom experiences the lowest strain owing to its farther distance from the tool.

Recrystallization Mechanism in Different Locations

During high-temperature deformation of the Al alloy, such as FSSP, the most common mechanisms for grains development, which are influenced by deformation temperature and strain rate, are dynamic recovery and dynamic recrystallization. Only dislocation annihilation and polygonization occur during dynamic recovery, and some new grains with high-angle grain boundaries appear during dynamic recrystallization (Ref 33). In the EBSD analysis of this research, the grains are defined as being “deformed” if the average boundary misorientation angle in a grain exceeds 2° . The grains which include in LAGBs, but whose internal boundary misorientation angle is below 2° are

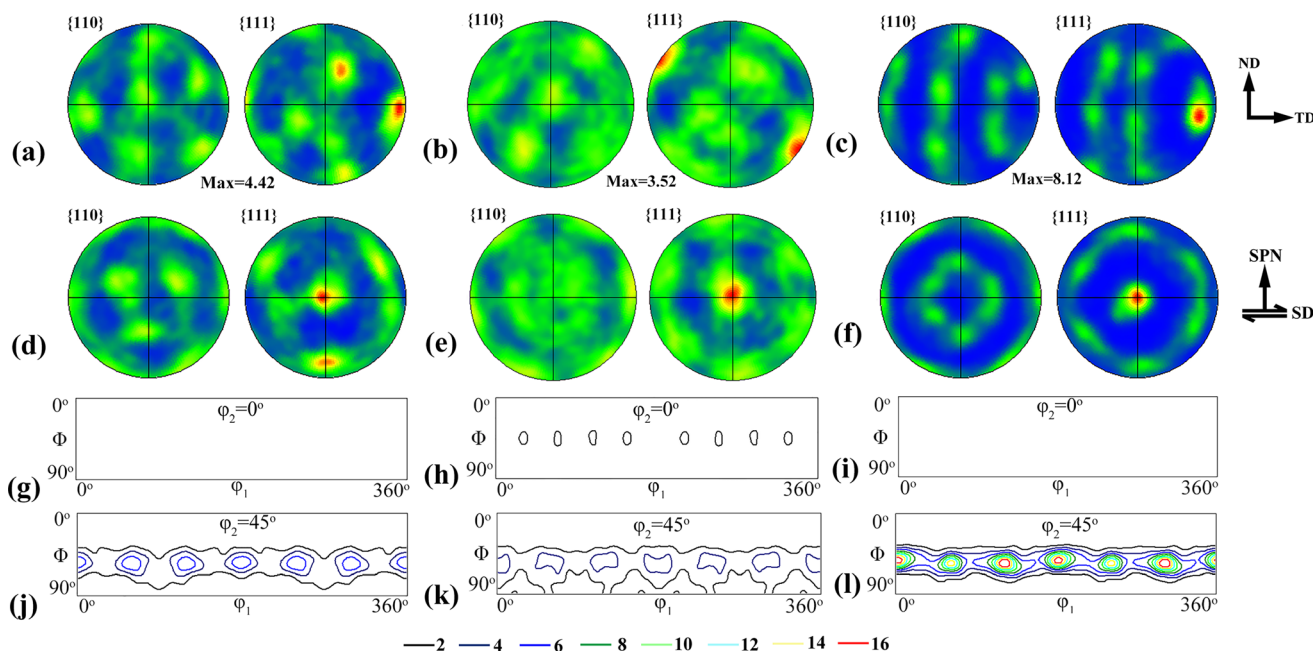


Fig. 7 PFs and ODFs in the (a, d, g, f) 1/8D, (b, e, h, k) 1/4D and (c, f, i, l) 3/8D of the SZ

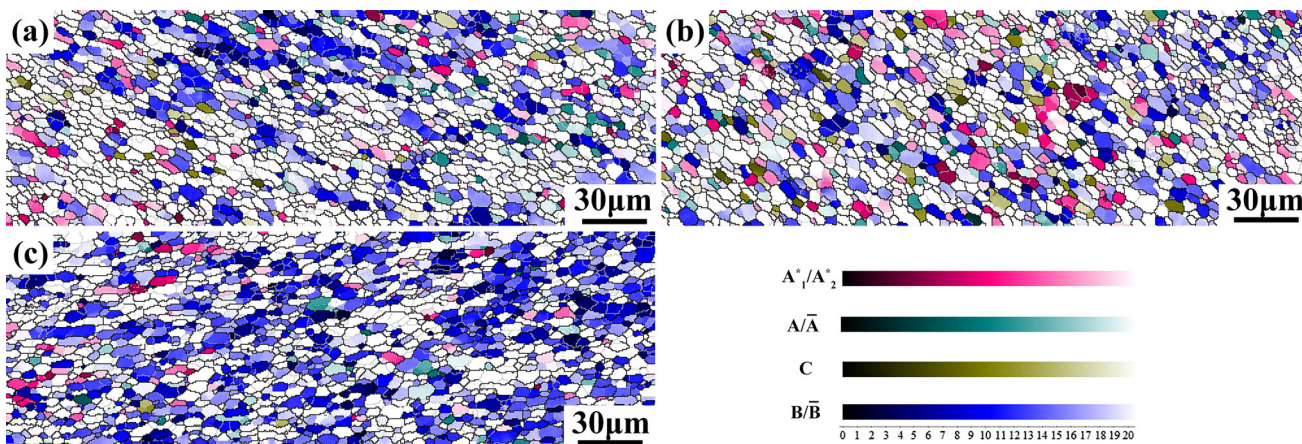


Fig. 8 Texture components developing in the (a) 1/8D, (b) 1/4D and (c) 3/8D of the SZ

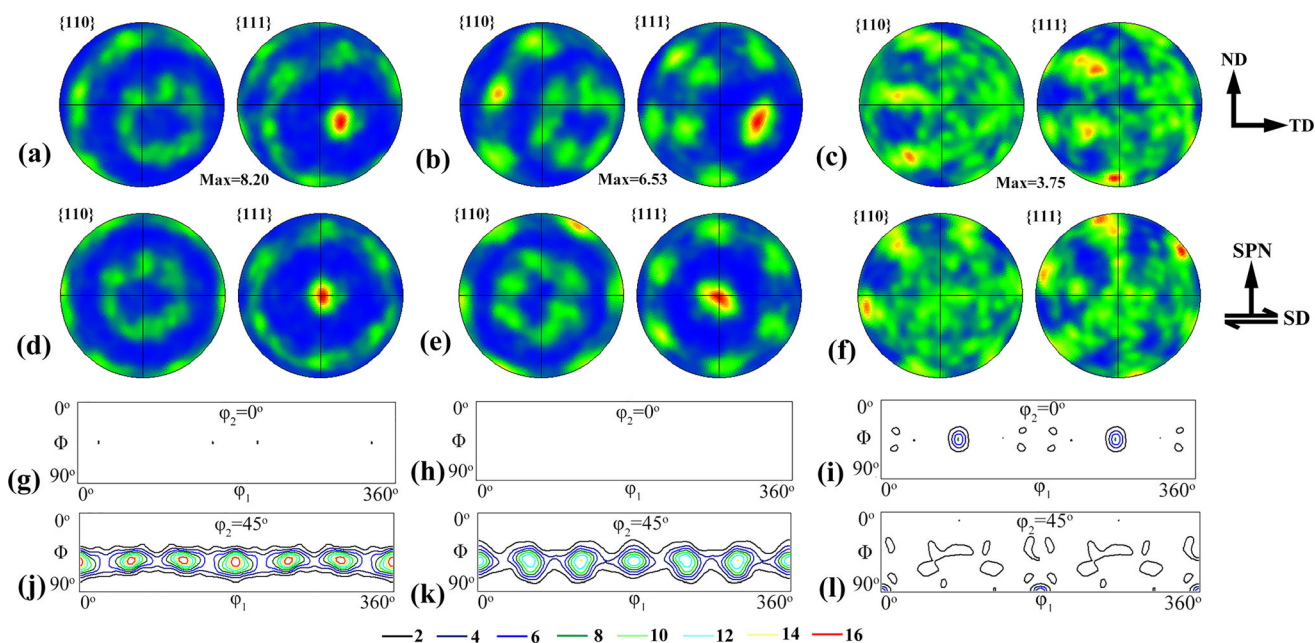


Fig. 9 PFs and ODFs in the (a, d, g, f) top, (b, e, h, k) middle and (c, f, i, l) bottom of the 1/2D of the SZ

classified as “substructured.” The remaining grains are categorized as “recrystallized.”

The evolution of the misorientation angle distribution from the BZ to the SZ is shown in Fig. 11. The LAGBs fraction in the BZ is very close to that in the as-deposited Al coating. Figure 12 shows the volume fraction variation of recrystallized grain from the BZ to the SZ. It can be clearly seen that the volume fraction of recrystallized grain in the BZ is nearly same with that in the as-deposited Al coating.

The LAGBs fraction dramatically decreases and the HAGBs fraction increases in the range from 32 to 57° in the HAZ, and new equiaxed grains without LAGBs have developed, which marked by dashed white ellipses in Fig. 3c. Compared to that in the as-deposited Al coating,

the volume fraction of recrystallized grain in the HAZ is slightly elevated. Due to the energy stored after deformation, new equiaxed grains in the HAZ of the cold rolling Al alloys could come from classical nucleation and grain growth during static recrystallization (Ref 34). High energy will store in the grains owing to the severely plastic deformation of the particles during cold spray process, which means that the recrystallization is easy to occur in the HAZ under the influence of heat during FSSP.

In the TMAZ, the LAGBs fraction further decreases in the range from 2 to 5° and the HAGBs fraction increases in the range from 40 to 57° as compared with that in the as-deposited Al coating. The volume fraction of recrystallized grain increases, which means that the dynamic recrystallization occurs in the TMAZ. It should be note that the

Fig. 10 Texture components developing in the (a) top, (b) middle and (c) bottom of the 1/2D of the SZ

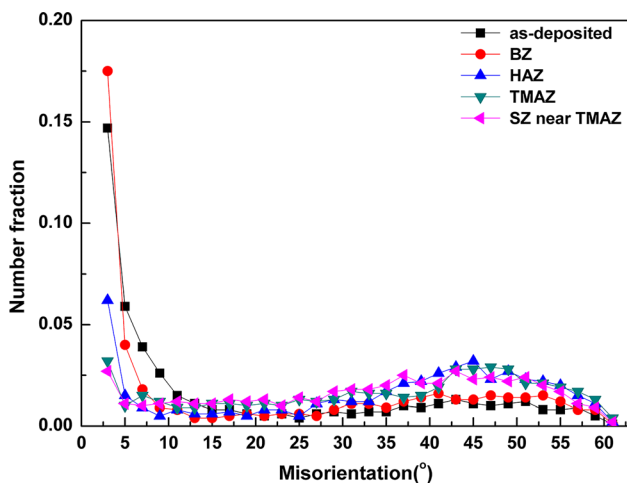
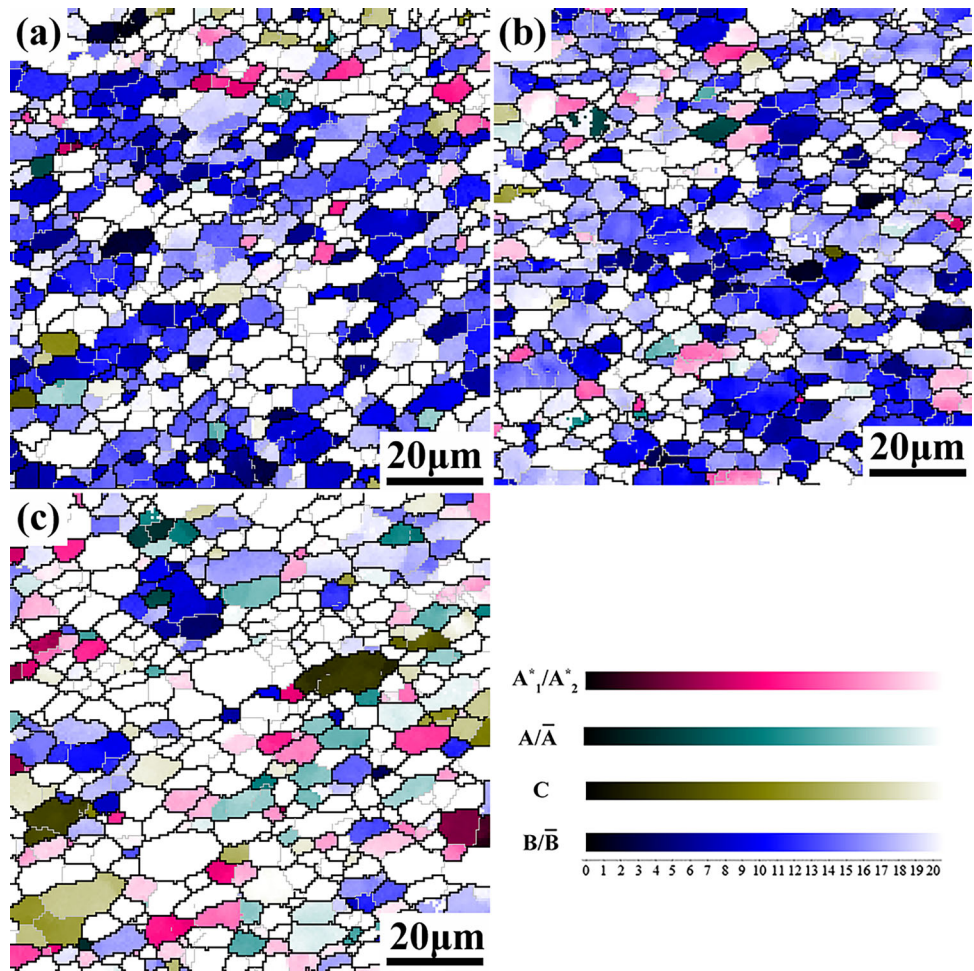


Fig. 11 Evolution of the misorientation angle distribution from the BZ to the SZ

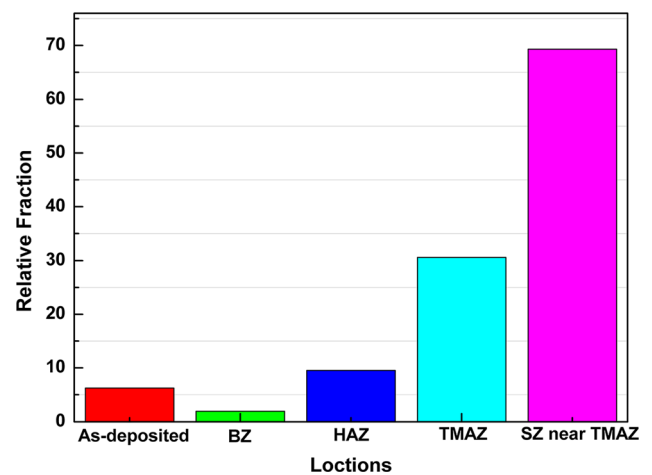


Fig. 12 Volume fraction variation of recrystallized grain from the BZ to the SZ

discontinuous dynamic recrystallization (DDR_X) and CDR_X could significantly increase the HAGBs fraction (Ref 21). The CDR_X usually associates with the grain rotation, due to the absorption of dislocations into the sub-

grain boundaries, which produces HAGBs with little boundary migration (Ref 35-37). The DDR_X is characterized as the nucleation of new grains at old HAGBs followed by grain boundary migration (Ref 38). From the

perspective of dynamic recrystallizations, the strain in materials deformed by slip and twinning may provide preferred nucleation sites and sufficient strain energy, thus promoting the dynamic recrystallizations of the microstructure (Ref 39, 40). Since a large number of sub-grains contain in the cold-sprayed coating before FSSP (Fig. 3a), the grains could more easily recrystallize. It is more likely that the CDRX with the rotation of sub-grains occurs in the TMAZ. Meanwhile, the serrated HAGBs and the elongated fibrous grains under subdivisions marked by dashed black ellipses can be observed in the TMAZ, indicating that the GDRX characterized by the grains elongation that reduces the spacing between the grains boundaries until they impinge and pinch off to form new grains also contributed to the grain development (Ref 41).

The fraction distribution of misorientation angle in SZ is almost the same as that in TMAZ shown in Fig. 11. Thus, the grains development in the TMAZ could provide more relevant information about the formation of ultrafine grains in the SZ, which figures that the CDRX and the GDRX both contribute to the grain development. The volume fraction of recrystallized grain further increases in the SZ, demonstrating that the dynamic recrystallization proceeds on more thoroughly.

Nano-Hardness and Elastic Modulus

Figure 13 gives the load-displacement curves of different locations of the SZ, and the nano-hardness and elastic modulus are shown in Table 2. The nano-hardness and elastic modulus of the cold-sprayed Al coating after FSSP is close to those of the Al bulk (Ref 42), indicating that FSSP is an effective way to enhance the mechanical properties of the coating. Moreover, the nano-hardness was different in various locations of 1/2D of the SZ. As the

depth of the 1/2D of the SZ increases, the penetration depth of the indentation increases first and then decreases. The 1/4D of the SZ has the similar penetration depth with the bottom of the 1/2D of the SZ. Therefore, the middle of the 1/2D of the SZ has the minimum plastic deformation, and the bottom of the 1/2D of the SZ and the 1/4D of the SZ have the maximum plastic deformation. As shown in Table 2, the nano-hardness of the top, middle, and bottom of the 1/2D of the SZ are 0.65 GPa, 0.69 GPa, and 0.55 GPa, respectively. The nano-hardness of the 1/4D of the SZ is found to be 0.50 GPa. Meanwhile, the top and middle of the 1/2D of the SZ have the similar elastic modulus. The elastic modulus is similar for the bottom of the 1/2D and 1/4 D of the SZ, but significantly decrease compared to the top and middle locations.

The nanomechanical property of the material mainly depends on its microstructure, including grain size, grain orientation and dislocation density. As the results from previous study (Ref 43), the grain orientation variation in the SZ has negligible effect on the hardness of the cold-sprayed Al coating after FSSP. Therefore, the main factors affecting the nano-hardness may be grain size and dislocation density in this study. The Nix-Gao model can be used to define the effect of grain size on the nano-hardness. As described by Nix-Gao model, a hemispherical plastic deformation zone with a radius “r” will be created when indentation test with the Berkovich indenter. Thus, the diameter of the plastic deformation zone can be calculated using Eq. (1) (Ref 44):

$$2r = 2a \approx 8.7h \tag{Eq 1}$$

where “r” represents the radius of the plastic deformation zone, “a” denotes the radius of the indentation, and “h” is the depth of the indentation. Through calculation, the radius of the plastic deformation zone is 4.26 μm, 4.18 μm, and 4.70 μm for the top, middle, and bottom of the 1/2D of the SZ, respectively. The radius of the plastic deformation zone is 4.87 μm for the 1/4D of the SZ. As given in Table 1, the average grain size in the middle of the 1/2D of the SZ is the same as that in the 1/4D of the SZ, but the LAGBs fraction is much higher, indicating that the aggregation of a large number of dislocations leads to smaller plastic deformation zone. The LAGBs fraction in the top of the 1/2D of the SZ is the same as that in the 1/4D of the SZ. However, the average grain size in the top of the 1/2D of the SZ is smaller, which also decreases the area of the plastic deformation zone. In summary, the grain size and dislocation interaction mechanism are the key factors affecting the nano-hardness within the SZ after FSSP.

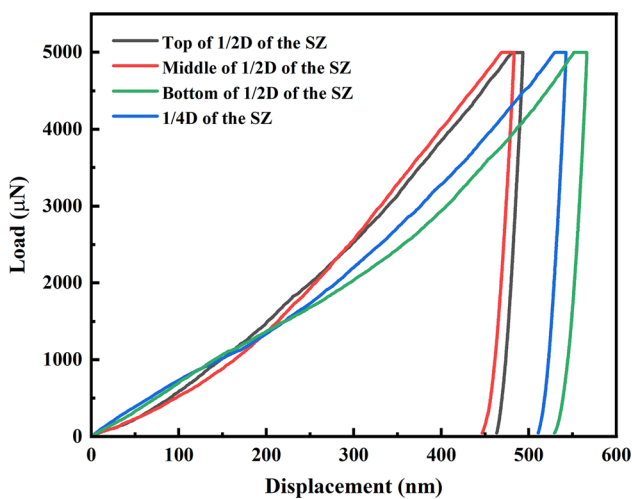


Fig. 13 Load-displacement curves of different locations of the SZ

Table 2 Nano-hardness and elastic modulus of different locations of the SZ

Locations	Nano-hardness, H, GPa	Elastic modulus, Es, GPa
Top of the 1/2D of the SZ	0.65	77.2
Middle of the 1/2D of the SZ	0.69	80.4
Bottom of the 1/2D of the SZ	0.55	70.9
1/4D of the SZ	0.50	68.8

Conclusion

FSSP was found to be an effective technique to modify the cold-sprayed Al coating. The grain structure, texture and nanomechanical properties of the cold-sprayed Al after FSSP were studied and following conclusions can be drawn from this research.

1. The average grain size in the cold-sprayed Al coating increases after FSSP. The LAGBs fraction and the density of the GNDs gradually decrease from the BZ to the SZ. From the top to the bottom of the 1/2D of the SZ, the average grain size gradually increases, while the LAGBs fraction and the density of the GNDs increase first and then decrease.
2. The main texture in the SZ is the B/\bar{B} component, the C component and the A_1^*/A_2^* components. The plasticized material flowed downward undergoes the highest shear strain according to the appearance of the highest B/\bar{B} component strength. The plasticized material experience higher shear strain in the top of the 1/2D of the SZ and lower shear strain in the bottom of the 1/2D of the SZ.
3. The features of grain development are found diverse in different locations. The static recrystallization mainly occurs in the HAZ, and the CDRX and the GDRX appear in the TMAZ. The formation of equiaxed grains in the SZ is a complex process, which is also driven by the CDRX and the GDRX.
4. The average nano-hardness of the cold-sprayed Al coatings after FSSP is 0.59 GPa, and the average elastic modulus is 74.33 GPa, which are similar to those of the pure Al bulk. The grain size and dislocation density are two key factors that influence the nano-hardness in the SZ after FSSP.

Acknowledgments This work was financially supported by the National Natural Science Foundation of China (No. 52101099), Innovation Capability Support Program of Shaanxi (No. 2023KJXX-082), Key Research and Development Program of Shaanxi (No. 2024GX-YBXM-344), Natural Science Basic Research Program of Shaanxi (No. 2024JC-YBMS-429).

References

1. T. Novoselova, S. Celotto, R. Morgan, P. Fox, and W. O'Neill, Formation of TiAl Intermetallics by Heat Treatment of Cold-Sprayed Precursor Deposits, *J. Alloys Compd.*, 2007, **436**(1-2), p 69-77.
2. M. Grujicic, J.R. Saylor, D.E. Beasley, W.S. DeRosset, and D. Helfritch, Computational Analysis of the Interfacial Bonding between Feed-Powder Particles and the Substrate in the Cold-Gas Dynamic-Spray Process, *Appl. Surf. Sci.*, 2003, **219**(3-4), p 211-227.
3. T. Suhonen, T. Varis, S. Dosta, M. Torrell, and J.M. Guilemany, Residual Stress Development in Cold Sprayed Al Cu and Ti Coatings, *Acta Mater. Acta Mater.*, 2013, **61**(17), p 6329-6337. <https://doi.org/10.1016/j.actamat.2013.06.033>
4. W.B. Choi, L. Li, V. Luzin, R. Neiser, T. Gnäupel-Herold, H.J. Prask, S. Sampath, and A. Gouldstone, Integrated Characterization of Cold Sprayed Aluminum Coatings, *Acta Mater.*, 2007, **55**(3), p 857-866.
5. Y. Tao, T. Xiong, C. Sun, L. Kong, X. Cui, T. Li, and G.L. Song, Microstructure and Corrosion Performance of a Cold Sprayed Aluminum Coating on AZ91D Magnesium Alloy, *Corros. Sci.*, 2010, **52**(10), p 3191-3197. <https://doi.org/10.1016/j.corsci.2010.05.023>
6. K. Balani, T. Laha, A. Agarwal, J. Karthikeyan, and N. Munroe, Effect of Carrier Gases on Microstructural and Electrochemical Behavior of Cold-Sprayed 1100 Aluminum Coating, *Surf. Coat. Technol.*, 2005, **195**(2-3), p 272-279.
7. Y.K. Wei, X.T. Luo, C.X. Li, and C.J. Li, Optimization of In-Situ Shot-Peening-Assisted Cold Spraying Parameters for Full Corrosion Protection of Mg Alloy by Fully Dense Al-Based Alloy Coating, *J. Ther. Spray Technol.*, 2017, **26**(1-2), p 173-183.
8. H. Bu, M. Yandouzi, C. Lu, and B. Jodoin, Effect of Heat Treatment on the Intermetallic Layer of Cold Sprayed Aluminum Coatings on Magnesium Alloy, *Surf. Coat. Technol.*, 2011, **205**(19), p 4665-4671. <https://doi.org/10.1016/j.surfcoat.2011.04.018>
9. R. Huang, M. Sone, W. Ma, and H. Fukanuma, The Effects of Heat Treatment on the Mechanical Properties of Cold-Sprayed Coatings, *Surf. Coat. Technol.*, 2015, **2015**(261), p 278-288.
10. D.I. Pantelis, P.N. Karakizis, N.M. Daniolos, in *Feasibility study of friction stir processing on thick aluminum cold sprayed coatings*, ed. by K.-D. Bouzakis, K. Bobzin, B. Denkena, M. Merklein. Proceedings of the 11th International Conference "THE-A" Coatings in Manufacturing Engineering, October 1-3, 2014 (Thessaloniki, Greece) (Laboratory for Machine Tools and Manufacturing Engineering (EEAM) of the Aristoteles University of Thessaloniki and of the Fraunhofer Project Center Coatings in Manufacturing (PCCM), 2014).
11. M. Grujicic, C.L. Zhao, W.S. DeRosset, and D. Helfritch, Adiabatic Shear Instability Based Mechanism for Particles/Substrate Bonding in the Cold-Gas Dynamic-Spray Process, *Mater. Des.*, 2004, **25**(8), p 681-688.
12. W.Y. Li, C. Yang, and H. Liao, Effect of Vacuum Heat Treatment on Microstructure and Microhardness of Cold-Sprayed TiN

- Particle-Reinforced Al Alloy-Based Composites, *Mater. Des.*, 2011, **32**(1), p 388-394.
13. H. Zhao, Q. Pan, Q. Qin, Y. Wu, and X. Su, Effect of the Processing Parameters of Friction Stir Processing on the Microstructure and Mechanical Properties of 6063 Aluminum Alloy, *Mater. Sci. Eng. A*, 2019, **751**(November 2018), p 70-79. <https://doi.org/10.1016/j.msea.2019.02.064>
 14. N. Nadammal, S.V. Kailas, J. Szpunar, and S. Suwas, Development of Microstructure and Texture during Single and Multiple Pass Friction Stir Processing of a Strain Hardenable Aluminium Alloy, *Mater Charact*, 2018, **140**, p 134-146.
 15. P.B. Prangnell and C.P. Heason, Grain Structure Formation during Friction Stir Welding Observed by the "Stop Action Technique," *Acta Mater.*, 2005, **53**(11), p 3179-3192.
 16. X. Wang, D. Zhang, J.T. Darsell, K.A. Ross, X. Ma, J. Liu, T. Liu, R. Prabhakaran, L. Li, I.E. Anderson, and W. Setyawan, Manufacturing Oxide Dispersion Strengthened (ODS) Steel Plate via Cold Spray and Friction Stir Processing, *J. Nucl. Mater.*, 2024, **596**, p 155076.
 17. P. Han, W. Wang, Z. Liu, T. Zhang, Q. Liu, X. Guan, K. Qiao, D. Ye, J. Cai, Y. Xie, and K. Wang, Modification of Cold-Sprayed High-Entropy Alloy Particles Reinforced Aluminum Matrix Composites via Friction Stir Processing, *J. Alloys Compoud.*, 2022, **25**(907), p 164426.
 18. F. Khodabakhshi, B. Marzbanrad, L.H. Shah, H. Jahed, and A.P. Gerlich, Surface Modification of a Cold Gas Dynamic Spray-Deposited Titanium Coating on Aluminum Alloy by using Friction-Stir Processing, *J. Ther. Spray Technol.*, 2019, **28**(6), p 1185-1198. <https://doi.org/10.1007/s11666-019-00902-z>
 19. F. Khodabakhshi, B. Marzbanrad, A. Yazdanmehr, H. Jahed, and A.P. Gerlich, Tailoring the Residual Stress during Two-Step Cold Gas Spraying and Friction-Stir Surface Integration of Titanium Coating, *Surf. Coat. Technol.*, 2019, **380**(October), p 125008. <https://doi.org/10.1016/j.surfcoat.2019.125008>
 20. R.W. Fonda, J.F. Bingert, and K.J. Colligan, Development of Grain Structure during Friction Stir Welding, *Scr. Mater.*, 2004, **51**(3), p 243-248.
 21. U.F.H.R. Suhuddin, S. Mironov, Y.S. Sato, and H. Kokawa, Grain Structure and Texture Evolution during Friction Stir Welding of Thin 6016 Aluminum Alloy Sheets, *Mater. Sci. Eng. A*, 2010, **527**(7-8), p 1962-1969. <https://doi.org/10.1016/j.msea.2009.11.029>
 22. S. Chen and X. Jiang, Texture Evolution and Deformation Mechanism in Friction Stir Welding of 2219Al, *Mater. Sci. Eng. A*, 2014, **612**, p 267-277. <https://doi.org/10.1016/j.msea.2014.06.014>
 23. J. Shen, S.B.M. Lage, U.F.H. Suhuddin, C. Bolfarini, and J.F. dos Santos, Texture Development and Material Flow Behavior During Refill Friction Stir Spot Welding of AlMgSc, *Metall. Mater. Trans. A Phys. Metall. Mater. Sci.*, 2018, **49**(1), p 241-254.
 24. D.X. Wei, Y. Koizumi, M. Nagasako, and A. Chiba, Refinement of Lamellar Structures in Ti-Al Alloy, *Acta Mater.*, 2017, **125**, p 81-97.
 25. D.X. Wei, Y. Koizumi, Y. Li, K. Yamanak, and A. Chiba, Sub-micron Lamellar Porous Structure Formed by Selective Dissolution of Ti-Al Alloy, *Mater. Des.*, 2016, **98**, p 1-11. <https://doi.org/10.1016/j.matdes.2016.02.096>
 26. Y.W. Chen, Y.T. Tsai, P.Y. Tung, S.P. Tsai, C.Y. Chen, S.H. Wang, and J.R. Yang, Phase Quantification in Low Carbon Nb-Mo Bearing Steel by Electron Backscatter Diffraction Technique Coupled with Kernel Average Misorientation, *Mater Charact*, 2017, **2018**(139), p 49-58. <https://doi.org/10.1016/j.matchar.2018.01.041>
 27. T. Liu, J.D. Leazer, and L.N. Brewer, Particle Deformation and Microstructure Evolution during Cold Spray of Individual Al-Cu Alloy Powder Particles, *Acta Mater.*, 2019, **168**, p 13-23.
 28. M. Li, R. Ma, Y. Ren, S. Chang, and L. Li, New Insights on Dislocation Forming Mechanism of Nickel-Based Superalloy Fabricated by Laser Powder Bed Fusion, *J. Mater. Res. Technol.*, 2024, **30**, p 4303-4309.
 29. Y.F. Sun, H. Fujii, N. Takaki, and Y. Okitsu, Novel Spot Friction Stir Welding of 6061 and 5052 Al Alloys, *Sci. Technol. Weld. Joining*, 2011, **16**(7), p 605-612.
 30. H. Azzeddine, D. Bradai, T. Baudin, and T.G. Langdon, Texture Evolution in High-Pressure Torsion Processing, *Progress Mater. Sci.*, 2022, **1**(125), p 100886.
 31. G.R. Canova, U.F. Kocks, and J.J. Jonas, Theory of Torsion Texture Development, *Acta Metall.*, 1984, **32**(2), p 211-226.
 32. R.W. Fonda, and J.F. Bingert, Texture Variations in an Aluminum Friction Stir Weld, *Scripta Mater.*, 2007, **57**(11), p 1052-1055.
 33. L. Zhen, H. Hu, X.Y. Wang, B. Zhang, and W. Shao, Distribution Characterization of Boundary Misorientation Angle of 7050 Aluminum Alloy after High-Temperature Compression, *J. Mater. Process. Technol.*, 2009, **209**(2), p 754-761.
 34. A.L. Etter, T. Baudin, N. Fredj, and R. Penelle, Recrystallization Mechanisms in 5251 H14 and 5251 O Aluminum Friction Stir Welds, *Mater. Sci. Eng. A*, 2007, **445-446**, p 94-99.
 35. J.Q. Su, T.W. Nelson, R. Mishra, and M. Mahoney, Microstructural Investigation of Friction Stir Welded 7050-T651 Aluminium, *Acta Mater.*, 2003, **51**(3), p 713-729.
 36. K. Jata and S.L. Semiatin, Continuous Dynamic Recrystallization during Friction Stir Welding of High Strength Aluminum Alloys, *Scripta Mater.*, 2000, **43**(8), p 743-749.
 37. B. Heinz and B. Skrotzki, Characterization of a Friction-Stir-Welded Aluminum Alloy 6013, *Metall. Mater. Trans. B*, 2002, **33**, p 489-498.
 38. C.G. Rhodes, M.W. Mahoney, W.H. Bingel, R.A. Spurling, and C.C. Bampton, Effects of Friction Stir Welding on Microstructure of 7075 Aluminum, *Scr. Mater.*, 1997, **36**(1), p 69-75.
 39. C.K. Yan, A.H. Feng, S.J. Qu, G.J. Cao, J.L. Sun, J. Shen, and D.L. Chen, Dynamic Recrystallization of Titanium: Effect of Pre-Activated Twinning at Cryogenic Temperature, *Acta Mater.*, 2018, **154**, p 311-324.
 40. L. Chai, B. Luan, D. Xiao, M. Zhang, K.L. Murty, and Q. Liu, Microstructural and Textural Evolution of Commercially Pure Zr Sheet Rolled at Room and Liquid Nitrogen Temperatures, *Mater. Des.*, 2015, **85**, p 296-308.
 41. H. Li, Y. Huang, and Y. Liu, Dynamic Recrystallization Mechanisms of As-Forged Al-Zn-Mg-(Cu) Aluminum Alloy during Hot Compression Deformation, *Mater. Sci. Eng. A*, 2023, **878**, p 245236.
 42. L. Zhang, T. Ohmura, S. Emura, N. Sekido, F. Yin, X. Min, and K. Tsuzaki, Evaluation of Matrix Strength in Ultra-Fine Grained Pure Al by Nanoindentation, *J. Mater. Res.*, 2009, **24**(9), p 2917-2923.
 43. G. Ji, H. Liu, G.J. Yang, C.X. Li, X.T. Luo, G.Y. He, and L. Zhou, Effect of Friction Stir Spot Processing on Microstructure and Mechanical Properties of Cold-Sprayed Al Coating on Ti Substrate, *Surf. Coat. Technol.*, 2021, **15**(421), p 127352. <https://doi.org/10.1016/j.surfcoat.2021.127352>
 44. W.D. Nix and H. Gao, Indentation Size Effects in Crystalline Materials: A Law for Strain Gradient Plasticity, *J. Mech. Phys. Solids*, 1998, **46**(3), p 411-425.

Publisher's Note Springer Nature remains neutral with regard to jurisdictional claims in published maps and institutional affiliations.

Springer Nature or its licensor (e.g. a society or other partner) holds exclusive rights to this article under a publishing agreement with the author(s) or other rightsholder(s); author self-archiving of the accepted manuscript version of this article is solely governed by the terms of such publishing agreement and applicable law.